This is a repository copy of *Selenium speciation in framboidal and euhedral pyrites in shales.*.

Article:

1   **Selenium speciation in framboidal and euhedral pyrites in shales**
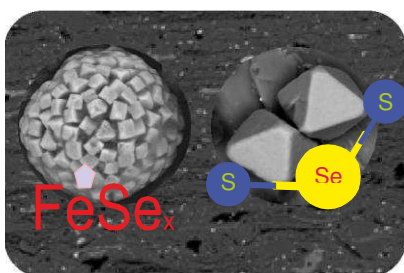
2

3   **Adriana Matamoros-Veloza*, Caroline L. Peacock and Liane G. Benning***

4   Cohen Geochemistry Laboratory, School of Earth and Environment, University of Leeds,

5   Leeds LS2 9JT, U.K

6

7   **ABSTRACT**

8   The release of Se from shales is poorly understood because its occurrence, distribution and

9   speciation in the various components of shale are unknown. To address this gap we

10   combined bulk characterisation, sequential extractions, and spatially resolved μ-focus

11   spectroscopic analyses and investigated the occurrence and distribution of Se and other

12   associated elements (Fe, As, Cr, Ni, and Zn) and determined the Se speciation at the μ-scale

13   in typical, low bulk Se containing shales. Our results revealed Se primarily correlated with

14   the pyrite fraction with exact Se speciation highly dependent on pyrite morphology. In

15   euhedral pyrites, we found Se(-II) substitutes for S in the mineral structure. However, we also

16   demonstrate that Se is associated with framboidal pyrite grains as a discrete, independent

17   $FeSe_x$ phase. The presence of this $FeSe_x$ species has major implications for Se release,

18   because $FeSe_x$ species oxidise much faster than Se substituted in the euhedral pyrite lattice.

19   Thus, such an $FeSe_x$ species will enhance and control the dynamics of Se weathering and

20   release into the aqueous environment.

21

INTRODUCTION

Selenium (Se) is an essential micronutrient but only within a very narrow concentration range, above which it is toxic.[1] Selenium is an antioxidant that prevents tissue damage and aids growth and metabolic processes,[2] however, an intake dose above 450 µg/day Se can disrupt dermal and neurological processes and ultimately be fatal.[3-4] The use of Se contaminated groundwaters for drinking and Se contaminated soils for agricultural purposes introduces Se into the human food chain. Se poisoning has been reported at several locations with extreme cases in China (Yutangba),[5] India (Punjab) and in Colombia (Villeta).[6-8] In order to help prevent future health hazards related to Se toxicity, we need to improve our understanding of the factors and mechanisms that control its fate and mobility in the environment.

A variety of geological and geochemical factors have been suggested as possible controls for the release of Se from rocks (e.g., rock type, weathering environment, groundwater composition, organic matter content, Fe or Se speciation etc.). [5,9-10] In Se-enriched surface environments, shales are an important source of Se to soils. [5,8,11-12] However, the transfer of Se from shale rocks into soils and groundwaters [5] and ultimately to humans via the food chain[6] is poorly constrained. Furthermore, the role of geological settings or specific geochemical reactions leading to the sequestration of Se in shale components are also poorly understood. This is because Se chemistry is highly complex. Selenium occurs in four principal oxidation states -II, 0, IV, VI, but Se(-I) compounds have also been found in nature and Se(II) compounds can be produced synthetically. Se has also six stable isotopes and is therefore of interest as a palaeo-environmental proxy.[12] The most oxidized species, Se(IV) and Se(VI), occur as the oxyanions selenite ($SeO_3^=$) and selenate ($SeO_4^=$), and they are the most soluble, reactive, bioavailable and therefore the most toxic Se species. Depending on their molecular bonding environment, different Se species have been suggested to be

47   associated (either surface adsorbed or structurally incorporated) with various possible Se

48   hosting phases.[13-15] In shales, the three main host components of Se are inferred to be

49   silicates, organic matter (OM) or sulfides (primarily pyrite). Organic matter (kerogen

50   fraction) has been suggested as a Se host in shales that are exceptionally Se and carbon rich,

51   and linked to coal beds.[15] However, neither the importance of OM as a Se host, nor a clear

52   correlation between Se and OM in typical black shales, with average lower Se concentrations,

53   have so far been demonstrated. Conversely, several studies proposed pyrite as the possible Se

54   host mineral in shales,[5, 8, 16, 17] yet a mechanistic or speciation related explanation is still

55   lacking. Experimental studies [18-21] suggested that Se is likely either adsorbed / reduced on

56   pre-formed pyrite grains or structurally incorporated into the sulfide phase. [22-23] However, a

57   detailed mechanistic reaction pathway that addresses the uptake of Se into pyrite during

58   pyrite growth, and a Se speciation and detailed structural and molecular bonding environment

59   regardless of pyrite formation pathways, is still lacking. This is despite the fact that pyrite is a

60   well-known sink for metals and, specifically, the accumulation of Se in shales may be used as

61   a tool to interpret palaeo-ocean chemical signals. [12, 21]

62   To better understand Se sequestration and speciation in shales, we examined the distribution

63   of Se and other elements (Fe, As, Cr, Ni, and Zn) in typical shales using bulk geochemical

64   and sequential extractions techniques and combined these with a detailed quantification of the

65   Se speciation in shale-associated pyrite grains at the μ-scale using synchrotron-based μ-X-ray

66   fluorescence (μ-XRF) and μ-X-ray absorption spectroscopy (μ-XAS). Our objectives were:

67   (1) to quantify the speciation and chemical environment of Se in shales (2) to demonstrate a

68   link between Se occurrence, distribution and sulfide morphology and (3) to derive likely

69   chemical pathways for both the accumulation and release of Se in / from shales.

70   **EXPERIMENTAL**

71   **Samples, bulk characterisation and Se analyses**

72 We characterized five shale samples from West Yorkshire, UK[24-25] (samples identified as

73 UK-1 to UK-5; **Table S1**). Powdered and homogenized samples were analysed for their

74 mineralogical composition (by X-ray diffraction, XRD), major elemental composition (by

75 bulk X-ray fluorescence, XRF), and trace element concentrations (by digestion and

76 inductively coupled plasma mass spectrometry, ICP-MS). Furthermore, we used elemental

77 analyses to determine total and organic carbon, total and reduced inorganic sulfur, and full

78 digestion and hydride generation atomic absorption spectroscopy (HG-AAS) to determine the

79 bulk Se content in each sample. The morphologies of sulfide grains in each sample were

80 identified using electron microscopy and Se concentrations in ~20-40 individual pyrite

81 grains, and a few control points (2-3) on the silicate and organic matter, were analysed by

82 electron microprobe (EMPA). Full details on the geological settings, the formation conditions

83 (i.e., redox etc.) and all methods employed are given in the Supplementary Information (SI).

84 **Sequential extractions and total digestions**

85 To quantify the Se concentrations associated with different shale fractions, we applied

86 various extraction protocols using a progressively stronger reagents that extract Se associated

87 with specific mineral and/or organic fractions.[16] Protocol A, consisted of a modified six-

88 fraction scheme[17]: water soluble (H_2O – Se(IV), Se(VI), organic-Se), ligand exchangeable

89 (K_2HPO_4/KH_2PO_4 – Se(IV) in oxides and clays), base soluble (NaOH - tightly bound Se(IV)

90 and selenides), elemental selenium (Na_2SO_3 – Se(0)), acetic acid soluble (CH_3COOH- Se in

91 calcite and gypsum) and residual ($HF/H_2O_2/HNO_3$ – Se in sulfides, recalcitrant organic

92 matter and in silicates).   Protocol B, followed a four-fraction scheme:[26] water

93 soluble/exchangeable (H_2O – Se(IV), Se(VI), organic-Se), oxides ($NH_2OH.HCl$ - hydrous Fe-

94 Mn oxides), sulfides/organics ($KClO_3$) and residual ($HF/H_2O_2/HNO_3$ – silicates, carbonates

95 and gypsum).   We also carried out a one-step extraction / reduction with $Cr(II)Cl_2$[27] to

96   quantify Se in diselenides and sulfides. The solutions resulting from each extraction step were

97   analysed for their Se contents using HG-AAS.[16]

98   **Se speciation**

99   Based on the results from the bulk and sequential analyses described above, we selected the

100   two samples with the highest bulk Se contents (UK-1 and UK-2) for the Se speciation

101   analyses using synchrotron-based μ-XRF and μ-XAS. Polished sections of both samples and

102   eleven standards (prepared as pressed pellets with 6% Se in boron nitride; CAS numbers and

103   chemical formulas in **Table S2** in SI) representing four Se oxidation states and Se-organic

104   species were analysed on beamline I18 at the Diamond Light Source Ltd, UK (full details of

105   beamline set up in SI).

106   Using μ-XRF we endeavoured to map in each sample ~ 3-5 areas of interest (100x100 μm,

107   150x150 μm or 350x450 μm). These areas contained various pre-identified pyrite

108   morphology assemblages and in each map the distribution of Se, Fe, Ni, Cu, Zn and As was

109   measured. The μ-XRF beam spot size was 5x6 μm, and the maps were collected using a step

110   size of 5 μm, and an integration time of 1000 ms. Despite multiple attempts we were only

111   able to collect statistically relevant data for sample UK-2, because the fluorescence signal to

112   quantify Se in sample UK-1 was too low. In the various areas of interest in sample UK-2 we

113   identified multiple points of interest (POI) representing either euhedral or framboidal pyrite

114   grains. At each of these POI twelve μ-X-ray absorption near edge spectra (μ-XANES)

115   collected at the same x and y coordinates confirmed there was no beam-induced sample

116   damage or changes in Se oxidation state as a result of μ-XANES measurement (**Figure S1**).

117   We then selected 14 specific POI that showed strong correlations between Se and the other

118   measured elements and recorded at each of these POI four μ-XANES scans with a step size

119   of 0.4 eV and beam spot size of 5x6 μm. From these 14 POI (**Table S3** in SI) only four gave

120   a Se absorption edge jump above 0.1 and we selected two POI for further μ-EXAFS analyses.

121   POIa was a typical euhedral pyrite grain and POIb represented framboidal pyrite grains. At

122   both POI we collected 16 µ-EXAFS scans at the Se K-edge.

123   The µ-XANES spectra were averaged, normalized, calibrated and compared with standards

124   using the inflection point of the first derivative, the position of the white line and the second

125   peak of the fingerprint as a reference. The energy of the monochromator was calibrated with

126   an Au foil and the K-edge energy for trigonal Se(0) was determined to be 12650 eV. Before

127   processing and analysis, our XANES and EXAFS data were calibrated to the theoretical

128   value for Se(0) of 12658 eV. The µ-EXAFS spectra were averaged, background subtracted

129   and fitted to various theoretical models. Initial fits using Se-C or Se-Se[28] bond distances

130   were unsuccessful and thus organic and elemental Se were discarded from the subsequent

131   fits. The remaining possibilities were either Se(-I) or Se(-II) most likely in sulphides and we

132   included several atoms (Fe, S and Se) and variable numbers of shells at close proximity to Se,

133   similar to the approach of Ryser et al.[29] Specifically, we trial fitted our spectra using the

134   models of pyrite[30] and marcasite[30] (FeS_2) and also ferroselite[31] ($FeSe_2$) but fits to

135   marcasite were not successful. We did not fit our spectra to dzharkenite (a ferroselite

136   polymorph FeS_2)[29] because this model has Se-Se distances of 2.28Å and our very first tests

137   showed no fit to Se-Se distances for the first shell. Further details of the µ-XANES and µ-

138   EXAFS data analysis are presented in sections 9 and 10 in the SI.

139   **RESULTS**

140   **Bulk composition and Se distribution in the various shale fractions**

141   The elemental and mineralogical analyses of all samples (**Tables S4-S6** and **Figure S2** in **SI**)

142   revealed the presence of high proportions of silicates (~44-96 %), and medium to low

143   contents of sulfides (~1-5 % pyrite, confirmed by the ~1-3 % reduced inorganic S contents)

144   and low total organic carbon contents (TOC = 2-5 %). Sample UK-5 was lacking pyrite (or

145 reduced S) and besides silicates, the second dominant phase was calcite. The bulk Se

146 concentrations varied between ~0.8 and ~10 µg/g with the highest values found in samples

147 UK-1 (3.13 ppm), UK-2 (9.77 ppm) and UK-5 (3.84 ppm). All samples were enriched in

148 trace elements (**Table S7** in **SI**) and Se significantly correlated with Ni (correlation

149 coefficient: 0.79), Cu (0.76), Cr (0.83) and V (0.81).

Se distribution

151 The sequential extraction results (**Table 1**, **Figure S3 and S4** in SI) are particularly

152 interesting for the samples with highest bulk Se concentrations. The base soluble and residual

153 fractions (protocol A) and the sulfide and organic fractions (protocol B) showed between

154 ~74-118% of the total bulk Se associated with sulfides or organic matter (**Table 1**, **Figure S4**

155 in SI). Sample UK-5 contained no inorganic sulfur or pyrite and was not further pursued. In

156 UK-1 and UK-2, the next extraction revealed that 50 and 74% respectively of the total Se was

157 sulfide associated, yet the remaining Se was not solely associated with organic matter (**Table**

158 **1** and **Figure S4** in **SI**).

Se in individual pyrite grains and the matrix

160 Samples UK-1 to UK-4 all contained pyrite as both euhedral and framboidal morphologies.

161 The Se concentration in individual framboidal or euhedral grains was typically ~ 1-3 orders

162 of magnitude higher than the bulk concentration (**Table 2**, and **Tables S8** in **SI**). Selenium in

163 "non-pyrite" control points (i.e., silicates and organic matter; total of 12 analyses in the 4

164 pyrite containing samples) was below detection, corroborating that pyrite was the prime

165 carrier of Se and cross-confirming the sequential extraction data (**Table 1**). Not surprisingly,

166 sample UK-2 (highest bulk Se content) showed the highest mean Se concentration in

167 individual grains (670 ppm). Although Se concentrations varied greatly between the two

168 morphologies or within the same morphological type in a single sample, overall Se

169   concentrations tended to be higher in euhedral grains (**Table 2** and **Table S8** in SI). Because

170   of the close link between shale pyrite weathering and Se release,[8,12,22-23,29] hereafter we

171   focussed our Se μ-XAS analyses solely on samples UK-1 and UK-2. These represent typical

172   shales containing pyrite and organic matter (**Table S6** in SI) and the highest bulk Se

173   concentrations among the samples studied.

Elemental distributions and correlations at the μ-level

175   From the five μ-XRF elemental maps in sample UK-2, two areas of interest (**Figure S5** in SI)

176   were selected for higher resolution μ-XRF mapping (**Figure 1**) and revealed statistically

177   significant correlations between Se, Fe, As, Ni and Cu (**Figure S6** and **Table S9** in SI) in the

178   pixels on or in close vicinity to pyrite grains.

Se oxidation states

180   The μ-XANES spectra of the 14 POI in the highest resolution μ-XRF maps in sample UK-2

181   revealed spectral fingerprints (inflection point of the first derivative, position of the white line

182   peak at the absorption edge) qualitatively similar to the seleno-L-cysteine, Se sulfide,

183   elemental Se and synthetic ferroselite[29] standards (**Figure S7 and S8**). Two particular areas

184   with framboidal (POIa) and euhedral grains (POIb) were selected for further μ-XANES

185   analyses (**Figure 2**). The X-ray energy at the inflection point in both POIa and POIb

186   (12658.5 eV) was very close to that in the Se(-II, 0) standards (12658.0 eV). The X-ray

187   energies at the peak of the white line (12660.6 eV for POIa and 12660.2 eV for POIb) were

188   also very similar to the standards (12660.2 eV for seleno-L-cysteine; 12660.2 eV for

189   elemental Se(0); 12659.7 eV for Se(-II) sulfide). On visual inspection, the spectral

190   fingerprints of POIa and POIb were very similar to the Se(-II) sulfide standard, and also

191   showed close similarity to the elemental Se(0) standard. POIa and POIb were however, less

192   similar to seleno-L-cysteine. Comparing with the synthetic ferroselite spectra, [29] the overall

193　fingerprint was similar. We did not align the Ryser et al. [29] spectrum with our spectra as the

194　details of beamline set up were unavailable, although, to the best of our knowledge, the

195　ferroselite spectrum was collected with a step size of 0.7 eV.[29] Despite the similarities

196　between POIa and POIb and Se(-II) sulfide, Se(-I) ferroselite and elemental Se(0), it was not

197　possible to determine the oxidation state, or the local coordination environment, of Se in our

198　samples as the uncertainty of the data at the XANES region was 0.4 eV and the XANES

199　spectra for the Se(-II) sulfide, Se(-I) ferroselite and elemental Se(0) standards are all visually

200　similar. Based on our comparisons we concluded from the μ-XANES data that the possible

201　Se oxidation states at both POI were Se(-II), Se(-I) or Se(0). Further differentiation in Se

202　speciation was achieved by fitting the μ-EXAFS data.

203　**Se chemical environment and bonding characteristics**

204　The μ-EXAFS spectra in k-space (**Figure 3**) indicated a similar local coordination

205　environment of Se for both POI (see also **Figure S9** in **SI** with overlaid POI spectra). The

206　spectra are similar over the entire k-space range, with features at ~ 4.2, 5.7 and 6.5 Å^{-1}

207　apparent in both spectra. However, the Fourier transforms indicate that Se was not present in

208　exactly the same bonding environment in POIa and b. Sample spectra exhibited noisier and

209　more complex oscillations compared to the standards (**Figure 3** and in **Figure S7** in **SI**) due

210　to the lower concentration of Se (max 670 ppm in euhedral grains; **Table 2**). The fingerprints

211　in k-space between both POI and the synthetic ferroselite,[29] showed that both spectra were

212　comparable in phase but with smaller oscillatory amplitudes at low wavenumbers. The

213　sample spectra were clearly out of phase with the seleno-L-cysteine, Se sulfide and elemental

214　Se standards (**Figure S7** and **S10** in SI).

215　Our fit of the POIa spectrum consisted of four single scattering paths (**Table 3** and **Figure 3**)

216　with bond distances consistent with those of S-S and S-Fe in pyrite (where S-S$_1$=2.18 Å, S-

217　Fe$_1$=2.26 Å, S-S$_2$=3.07 Å, and S-S$_2$=3.32 Å) [30], but invoking a substitution of S by Se [30]

218   that resulted in a local expansion of 8 % in the first shell (Se-S$_1$) and 4 % in all the others.

219   The sum of the modelled bond distances (11.351 Å) is very close to that of the pyrite

220   structure (10.830 Å), however it is expanded as a result of S substitution with Se, where Se

221   has a larger atomic radii compared to S. POIb data were fitted (**Table 3**) using five single

222   scattering paths, four corresponding to the theoretical structure of ferroselite[31] (Se-Fe$_1$=2.35

223   Å, Se-Fe$_2$=2.38 Å, Se-Se$_2$=3.40 Å and Se-Se$_3$=3.58 Å) and one single scattering path (Se-

224   S=3.07 Å) corresponding to the pyrite structure.[30] The first two Se-Fe paths contributed

225   entirely to the first peak of the Fourier transform (involving 3 Fe atoms, **Table 3**) and the

226   remaining two Se-Se paths plus the Se-S path contributed to the second peak (individual path

227   contributions in **Figure S11** in SI). The Se-Fe bond distances (average 2.31 Å) are shorter

228   than in the theoretical structure of ferroselite[31] (average 2.37 Å, Se-Fe=2.35Å with one Fe

229   and Se-Fe=2.38Å with 2 Fe) and are also shorter than in the fit to synthetic ferroselite

230   reported by Ryser et al. [29] (Se-Fe average 2.38 Å). We attribute our somewhat short Se-Fe

231   bond distance to the fact that we are fitting a complex natural sample that likely slightly

232   differs in crystal structure to a theoretical model or indeed a synthetic precipitate. In fact,

233   Ryser et al. [29], when fitting Se in their sample, fit to a ferroselite polymorph (dzharkenite)

234   with a first shell attributed to Se-Se at an average bond distance of 2.28 Å but our fit showed

235   no Se-Se bonds in the first shell.

236   We performed Se speciation analysis on POI clearly identified as pyrite and expected the

237   local coordination environment to reflect structural Se substitution for S as previously

238   suggested. [22-23] However, our μ-EXAFS analysis (**Table 3** and **Figure 3**) suggested that the

239   Se coordination environment in pyrite was dependent on the pyrite morphology. In euhedral

240   grains (POIa) Se was substituted for S in the pyrite structure as previously suggested, but in

241   framboidal grains (POIb) the local environment of Se was akin to Se in a discrete ferroselite-

242   like species (FeSe$_x$).

243 **Table 1.** Concentration of Se (µg/g) in the principal fractions in the shale samples as derived through application of protocol A and B and the

244 Cr(II)Cl$_2$ extraction; in brackets shown are the % Se in each fraction as a fraction of the total bulk Se.

		Protocol A - Se(µg/g), (%)[a]			Protocol B - Se(µg/g), (%)[a]	Se(µg/g)
		Base soluble	**Residual**		**Sulfides + Organics**	
					Sulfides and Organics	
	Bulk Se µg/g	Tightly bound Se(IV), organic and inorganic selenides	Sulfides, recalcitrant organic matter, silicates	% OM+Sulfides[b]		Se in Sulfides Cr(II)Cl$_2$
UK1	3.13	2.48 (79)	0.29 (9.9)	88	3.70 (118)	1.57 (50)
UK2	9.77	6.51 (67)	2.80 (29)	96	9.43 (97)	7.22 (74)
UK3	1.29	0.71 (55)	0.25 (19)	74	1.00 (77)	0.59 (46)
UK4	0.83	0.27 (33)	0.49 (59)	92	0.78 (94)	0.17 (20)
UK5	3.87	3.47 (90)	0.17 (4.4)	94	3.63 (94)	

245 [a] Percentage of Se in the extraction in relation to the bulk Se, %= (Fraction *100)/Bulk Se

246 [b] Sum of % Se base soluble + residual

247 **Table 2.** EMPA analysis of Se (ppm) in individual pyrite grains (with morphological splits) compared to bulk Se concentrations (UK-5

248 contained no pyrite; see also **SI Table S3** and **S4**). Left, middle and right panels include basic statistics for Se concentrations with no

249 differentiation in morphology, vs. framboidal and euhedral pyrites, respectively.

Sample	Se bulk ppm	Se, ppm individual grains (undifferentiated)				Se, ppm individual grains, framboidal aggregates				Se, ppm individual grains, euhedral			
		Mean	Min.	Max.	Number of analysed points (*)	Mean	Min.	Max.	Number of analysed points (*)	Mean	Min.	Max.	Number of analysed points (*)

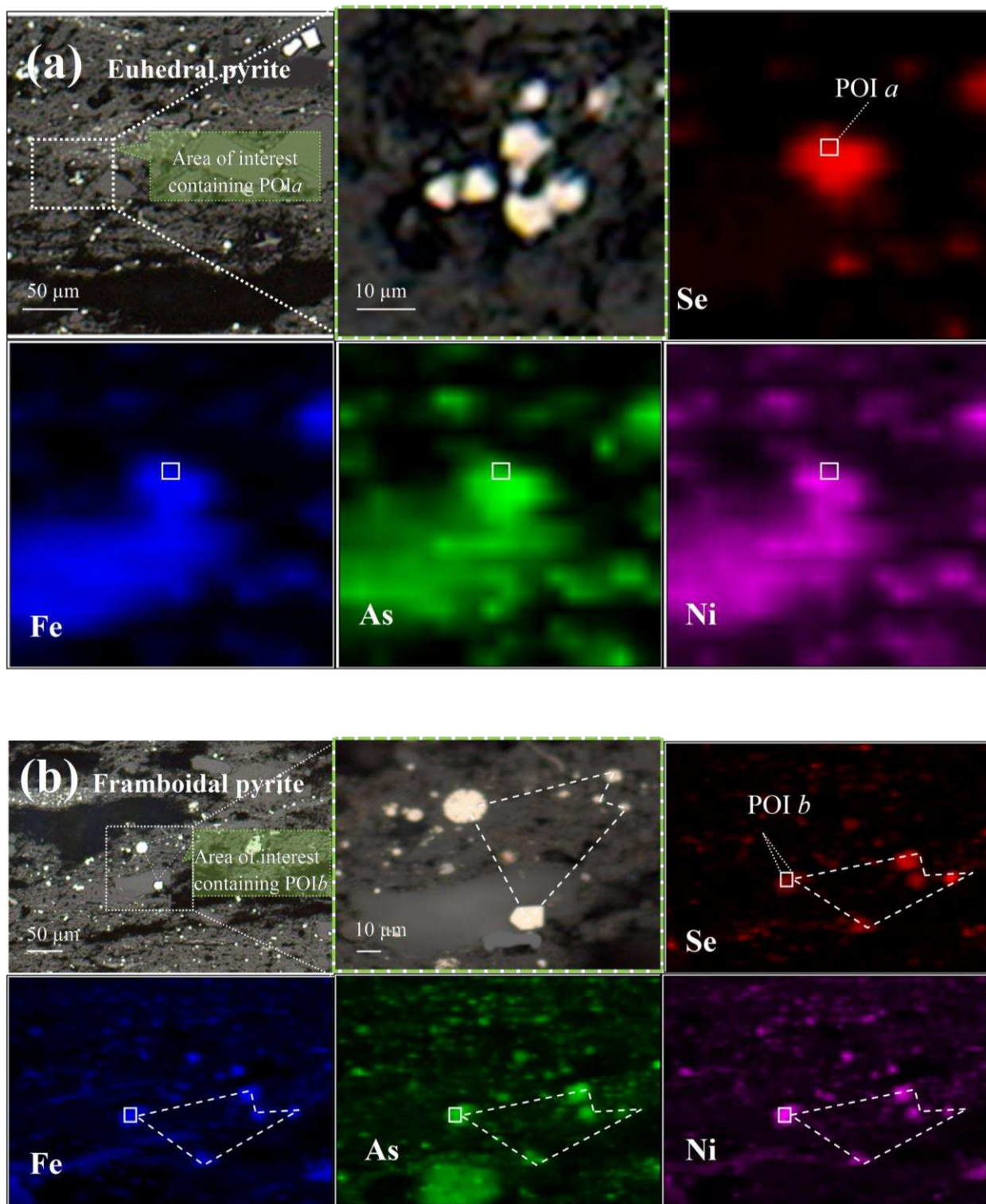|												
UK-1	3.13	255	100	561	29 (<DL=5)	192	110	300	15 (<DL=5)	661	100	561	14
UK-2	9.77	365	110	670	42 (<DL=8)	309	110	510	27 (<DL=6)	413	190	670	15 (<DL=2)
UK-3	1.29	171	110	310	20 (<DL=12)	171	110	310	20 (<DL=12)	-	-	-	0
UK-4	0.83	164	120	200	26 (<DL= 17)	-	-	-	12 (<DL= 12)	164	120	200	11 (<DL=2)

250   *DL= Limit of Detection, 90 ppm; points below DL were excluded from the statistical analyses.

251   **Table 3.** Local coordination environment of Se at POIa and b as determined by Se K-edge

252   μ-EXAFS analysis.

	Path	N^a	R (Å)^b	σ^2 (Å^2)	R-factor	χ^2
POIa$_{euhedral}$	Se-S	1	2.344 ± 0.003	0.003	0.024	205
	Se-Fe	3	2.354 ± 0.003	0.004		
	Se-S	6	3.198 ± 0.003	0.018		
	Se-Se	4	3.455 ± 0.003	0.018		
POIb$_{framboidal}$	Se-Fe	1	2.284 ± 0.004	0.005	0.022	92
	Se-Fe	2	2.318 ± 0.004	0.005		
	Se-S	2	2.987 ± 0.004	0.009		
	Se-Se	4	3.308 ± 0.004	0.002		
	Se-Se	6	3.479 ± 0.004	0.002		

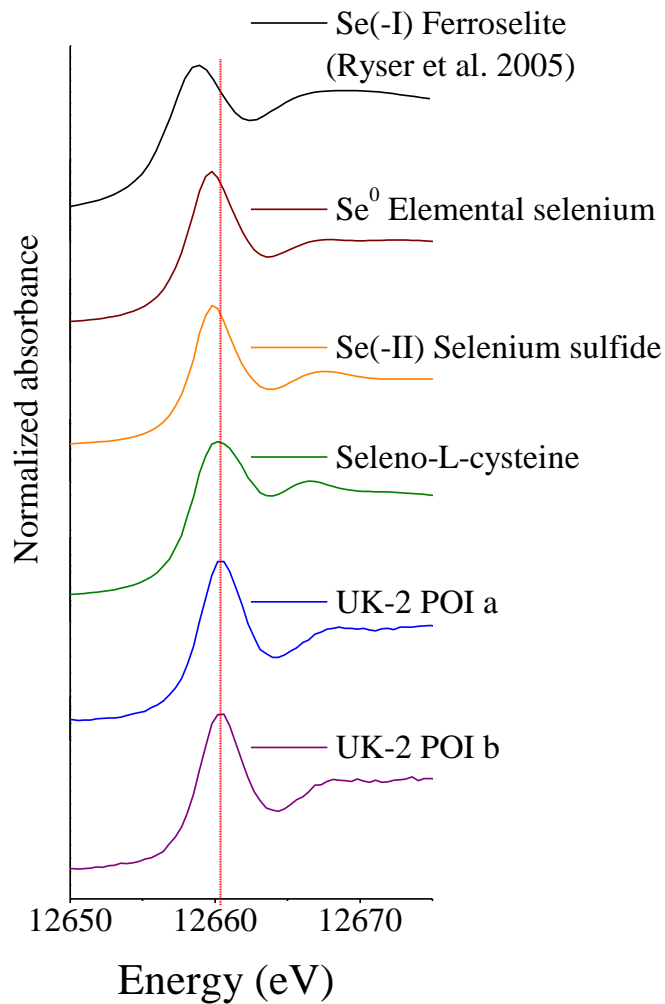253   [a] Degeneracy (coordination number for single paths)

254   [b] Inter-atomic distances

255

Figure 1. Ligth microphotographs of the μ-XRF areas of interest and corresponding μ-XRF elemental maps around POIa (top) and POIb (bottom). The enlarged areas next to them were imaged using the microscope on the beamline set at 45 degrees, hence the slight offset. Similarly, the distortion between these enlarged area images and the X-ray maps is due to the fact that the beamline camera and the incident X-ray beam see the sample at different

261   incident angles. In the enlarged image and the X-ray maps for POI b the dotted lines are just

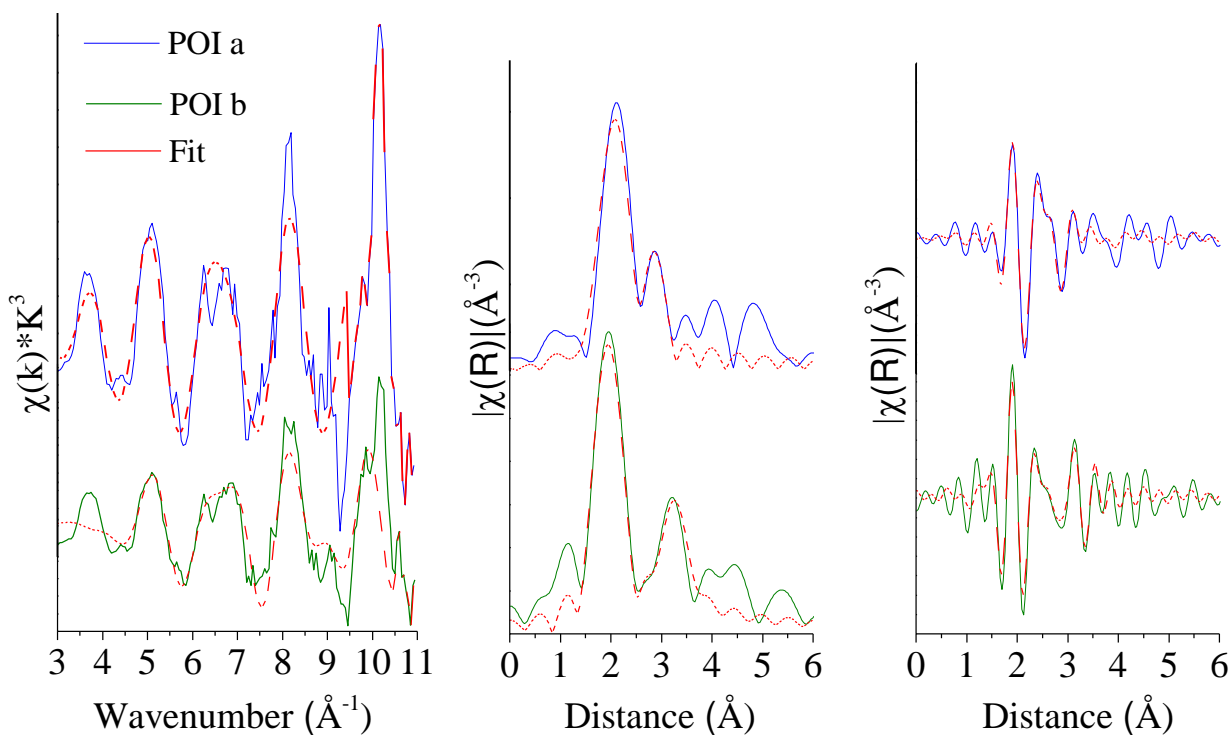262   to guide the eye and show the distortion.

263

264

265   **Figure 2.** Se K-edge μ-XANES spectra from POI a and b and selected standards. We also

266   included the Se(-I) ferroselite standard from Ryser et al. [29] but note that the spectral position

267   in this spectrum is offset, yet the general shape and amplitude of the spectrum can be

268   compared with our data.

269

270

Figure 3. Averaged k^3-weighted (left plot) experimental data and fits (dashed lines) for POI a (top) and POIb (bottom), real part of the Fourier transform of the spectra (middle) and fits using a k-weight of 3 (right).

DISCUSSION

Se in shales and in the pyrite fraction

The UK samples are typical shale rocks with relatively low bulk Se concentrations (<1 to ~ 10 µg/g). Sequential extractions, microprobe analyses and µ-XRF data clearly demonstrated that the main Se host in these samples was pyrite, with sequential extraction also suggesting minor Se associated with organic matter. As such our results strengthen previous data [32-34] that reported Se in carbonaceous shales highly associated with pyrite and organic matter. In the highest bulk Se samples (UK-1 and UK-2), 50 and 74% of the Se (**Table 1**) was associated with pyrite, and µ-XRF maps only showed high Se values on pyrite and low Se values in the organic matter or silicates matrix, corroborating the minor Se-organic matter association. The strong µ-scale correlations between Se, As, Ni and Cu in the pyrite grains also confirm the Se-pyrite link, as these metalloids and metals are most often solely enriched in pyrite and not in organic matter.[32, 35] Of crucial importance, our results also show that variations in total Se concentrations in typical shales do not solely depend on total S and organic C contents, but in addition there is a clear link between Se concentration and pyrite grain morphology (**Table 2** and **Table S6**). Microprobe analyses showed that euhedral pyrites contained overall far higher concentrations of Se compared to framboidal pyrites (**Table 2** and **Table S8** in SI) and that in fact no (< 90 ppm detection limit) Se was associated with any organic matter or silicate grains. There is an apparent mismatch between the proportion of Se associated with non-pyrite fractions in the sequential exactions **(Table 1)** and the absence of Se in the non-pyrite matrix measured with the microprobe. This is because sequential extractions measure bulk Se which is diffusely distributed in the non-pyrite matrix, while microprobe point analyses will only show high values in localised grains (i.e., pyrite), where Se is highly concentrated. In Matamoros et al.[16] we demonstrated that even if organic C contents (2-5 %) were higher than pyrite contents (1-3 %), Se was still preferentially

300   associated with pyrite. Thus the data in our current study, combined with literature

301   knowledge about pyrite formation pathways[35-40] helps us understand how Se is sequestered

302   into, and released from, pyrite in shales.

303   **Pyrite formation in shales and links to Se speciation**

304   The grain-level concentrations and speciation of Se depended on whether pyrite was present

305   in framboidal or euhedral morphology (**Table 2**, **Table 3** and **Table S8**). This difference can

306   be attributed to variations in chemical environments and formation pathways of the two

307   morphologies, or the effects of diagenesis.[41]

308   In natural settings framboidal pyrite is known to form rapidly at the chemocline where Fe and

309   S sources are readily available.[36-38] Here Se will be present as an oxic species, in either

310   aqueous or sorbed form.[18-20] Framboids are difficult to synthesise in the laboratory[39] and no

311   experimental evidence on Se-framboidal interactions is available. Some experimental studies

312   used iron sulfides (e.g., mackinawite,[42] pyrite[18-20, 43]) and sorbed Se onto them. When

313   synthetic pyrite was used, the Se was co-reduced leading to the formation of ferroselite

314     $FeSe(-I)_x$.[18,42,44]   Our current Se-edge μ-XAS data on natural framboids shows an

315   independent ferroselite-like $FeSe(-I)_x$ species as the dominant Se form associated with our

316   framboids (**Figure 3**). Combining the experimental evidence with our μ-XAS data suggests

317   that co-reduction during framboid formation must be the dominant pathway to producing

318   ferroselite in natural framboidal pyrites formation environments.

319   Euhedral pyrite grains form more slowly via the supply of low levels of external, less reactive

320   Fe and Se.[35,45-48] The source for these Fe/Se species is diffusive transport, followed by their

321   reduction and subsequent sequestration into the euhedral crystal structure.[23,49] Our μ–XAS

322   data (**Figure 3**) clearly shows a Se for S replacement in our euhedral pyrite, supporting the

323 slow growth by coupled diffusion / reduction, which also leads to higher average Se

324 concentrations in euhedral grains (**Table 2**).

325 If such euhedral grains formed through framboidal aggregate re-crystallization,[36,46-47] we

326 would expect Se to retain the ferroselite, $FeSe(-I)_x$ speciation as in the framboids. However,

327 this is not the case as our euhedral POIa µ-XAS evidences Se replacing S in the pyrite

328 structure (**Figure 3** and **Table 3**).

329 We demonstrated that Se speciation in pyrite in shales is dependent on pyrite morphology but

330 further spatially resolved speciation studies in other shale samples are necessary to evaluate if

331 such a morphology-dependent speciation is universal, or only linked to pyrites formed

332 through similar sedimentary processes. [47-48]

333 **The formation and importance of $FeSe_x$ species in framboidal pyrite**.

334 In modern marine sediments the most frequent pyrite morphology is framboidal [50] and we

335 demonstrate Se in this morphology to exists as ferroselite, which is thermodynamically stable

336 over a wide range of pH and low oxygen conditions (**Figure S12** left in **SI**).

337 The formation of ferroselite has been studied experimentally under both abiotic and biotic

338 conditions. Naveau et al. [18] investigated the adsorption of aqueous Se (IV) and Se(-II) onto

339 natural and synthetic pyrites and showed that Se is first reduced in solution and then it

340 adsorbs onto the pyrite surface. This reduction must be counterbalanced by the oxidation of

341 reduced iron species in pyrite. Charlet et al.[43] demonstrated that ferroselite ($FeSe_2$) and Se(0)

342 can form when reacting synthetic nanophase pyrite with Se(IV) and Se(VI) solutions.

343 However, in another study from the same group [19] the reduction of aqueous Se(IV) by pyrite

344 was corroborated, but the formation of ferroselite was excluded, instead elemental selenium

345 was suggested as the Se species at slightly acidic and neutral pH (4.5 - 6.6). The ability of

346 other ferrous minerals (e.g., green rust, mackinawite, siderite or troilite) to reduce aqueous

347 Se(IV) and Se(VI) to elemental Se and selenides has been inferred to be coupled to the

348 oxidation of S(-II)/Fe(II) to S(0)/Fe(III) in such phases.[20,42-44,53-54] Other evidence suggests

349 microbial metabolic processes may be responsible for the formation of selenides[53-54] and

350 ferroselite in particular. Herbel et al.[53] using XAS analyses of selenite-respiring bacteria

351 showed initially a microbial reduction of selenite to elemental Se and a further reduction to

352 Se(-II) species and the formation of $FeSe_x$ precipitates.

353 Combining these observations with our results, we suggest that in our shale sample the $FeSe_x$

354 species formed coevally with the framboids at the chemocline where microbial processes

355 dominate and through reduction of local aqueous Se. During subsequent diagenesis or

356 weathering $FeSe_x$ will be highly soluble at low pH and intermediate redox conditions (**Figure**

357 **S12** in **SI**), thus allowing for easy Se release and subsequent transport or re-adsorption onto

358 other minerals.

359 **Implications for Se release**

360 Our Se mobility data from the sequential extractions showed Se easily liberated from oxides,

361 clay minerals and carbonates. When reacting our samples with mildly acidic reagents

362 (Protocol A: water, exchangeable, Se(0) and acetic extractions – **Figure S3** in SI) 10 % of the

363 total Se was easily released. In a weathering environment characterised by slightly acid to

364 neutral pH's, this will certainly release Se from shales into local groundwaters. The largest

365 proportion of Se however, was associated with pyrite, which is the largest and most reactive

366 Se host phase in shales. Oxidative pyrite weathering from shales together with dissolution of

367 the more soluble $FeSe_x$ will therefore control the delivery of Se to aquifers and/or soils.

368 Specifically, such dissolution processes result in the redistribution of iron into Fe

369 oxyhydroxides (e.g., ferrihydrite) or Fe oxyhydroxide sulfates (e.g., schwertmannite) and the

370 production of sulfuric acid leading to acidic[55] soils. The associated Se species ($FeSe_x$ and Se

371 in the euhedral pyrite structure) will co-oxidise to form elemental Se and with further

372   oxidation these will convert to more toxic and bioavailable selenite or selenate species[6,8]

373   (**Figure S12** right in **SI**). Selenite species behave analogously to As species[56-58] when

374   interacting with minerals and thus once in the aqueous medium, selenite may re-adsorb onto

375   FeOOH particles at acidic pH conditions, or remain bioavailable as free aqueous species in

376   aquifers and thus be transferred to the human food chain with harmful effects.

377   The rates at which the different pyrite morphologies are oxidised during shale weathering

378   will govern the release rates of Se, because framboidal pyrites (made of microcrysts with a

379   large surface area) are weathered faster than euhedral often larger pyrites crystals. Thus, in

380   shales with high framboidal pyrite contents[50] that are oxidatively weathered, Se release will

381   be maximal where secondary iron minerals that can sequester the released Se are limited

382   and/or where ambient pH is neutral to alkaline.

383   **Se as potential proxy for past environmental conditions**

384   Framboid size distribution is an often used proxy for redox conditions in marine

385   sediments[50]. Recently, the use of Se isotopes was suggested as another powerful palaeo-

386   environmental proxy.[5,12,59] Specifically, Mitchell et al.[12] suggested a link between bulk

387   Se/TOC ratios (mol/mol) and Se isotopic values as a first step towards such a proxy. They

388   also noted that the lack of Se speciation information is hindering the full use of Se isotopes as

389   a palaeo-proxy. We did not analyse the Se isotope compositions in our shales, but our bulk

390   Se/TOC ratios (**Table S6** in **SI**) varied between 2.48×10^{-6} and 8.74×10^{-5}, which lie within

391   the typical range suggested for shales[12] Our data shows a clear link between Se and pyrite

392   and a clear difference in Se speciation in framboidal and euhedral grains. Such a host-fraction

393   differentiation and a morphology-resolved speciation analyses, albeit difficult and time

394   consuming, could much improve the use of Se as a palaeo-environmental proxy. Therefore,

395   we infer that to demonstrate the power of Se as a potential proxy in both modern and ancient

396   settings, measuring only bulk Se isotopic values of rocks are insufficient. In a first step

397 towards a better Se palaeo-proxy, we propose that bulk Se isotopic analyses need to be

398 combined with spatially and morphologically resolved Se speciation analyses as described in

399 the current study. A further step – that may currently not yet be feasible technologically -

400 would be a spatially and host-fraction differentiated and also pyrite morphology-resolved Se

401 isotopic fingerprinting, combined with co-resolved Se speciation analyses. Such a combined

402 approach would indeed pave the way to a very powerful Se palaeo-oceanographic proxy.

403 **ASSOCIATED CONTENT**

404 **Supporting Information**

405 Sample details; bulk characterisation; Se distribution from sequential extractions and trace

406 elements; euhedral and framboidal pyrite microprobe analyses; correlation plots of μ-XRF

407 areas; details of μ-XANES and μ-EXAFS analyses; thermodynamic modelling. This

408 information is available free of charge via the Internet at http://pubs.acs.org.

409 **CORRESPONDING AUTHOR**

410 *E-mail: A.MatamorosVeloza@leeds.ac.uk; L.G.Benning@leeds.ac.uk; phone: +44 113

411 3435220; fax: +44 113 3435259.

418 **REFERENCES**

419 (1) Schrauzer, G.N.   Selenomethionine.   A review of its nutritional significance,
420   metabolism and toxicity. J Nutr. **2000**,130,1653-1656.

421   (2)   British   Nutrition   Foundation;
422   http://britishnutrition.org.uk/home.asp?siteld=43&sectionld=s

423   (3)   Vinceti, M., Nacci, G., Rocchi, E., Cassinadri, T. , Vivoli,R. Marchesi, C., Bergomi,
424   M. Mortality in a population with long term exposure to inorganic selenium via
425   drinking water. J Clin Epidemiol. **2000**, 53,1062-1068.

426   (4)   Nuttall, K.L. Review: Evaluating Selenium Poisoning. Ann of Clin Lab Sci. **2006**,
427   36(4), 409-420.

428   (5)   Zhu, J., Johnson, T.M., Clark, S.K, Zhu, X., Wang, X. Selenium redox cycling during
429   weathering of Se-rich shales: A selenium isotope study. Geochim Cosmochim Ac.
430   **2014**, 126, 228-249.

431   (6)   Winkel, L., Johnson, A., Lenz, M., Grundi, T., Leupin, O.X., Amini, Manouchehr,
432   Charlet, L. Environmental Selenium Research - from Microscopic Processes to Global
433   Understanding. Environ Sci Technol. **2011**, 46(2), 571-579.

434   (7)   U.S. Department of Human Health and Services. Toxicological profile for selenium,
435   P.H. Service and A.f.T.S.a.D. Registry, Editors. Department Health and Human
436   Services. Public Health Service. Agency for Toxic Substances and Disease Registry.
437   2003.

438   (8)   Plant, J.A. Kinniburgh, P.L., Smedley, P.L., Fordyce, F.M. and Klinck, B.A. Arsenic
439   and Selenium In: Holland, H.D. and K.K. Turekian. Treatise on geochemistry. Vol. 9
440   Amsterdam ; London: Elsevier-Pergamon. 2003.

441   (9)   Bar Yosef, B. Selenium desorption from Ca-kaolinite. Commun Soil Sci and Plan.
442   **1987**, 18(7), 771-771.

443   (10)   Zawislanski, P.T., Benson, S.M., Terberg, R., Borglin. S.E. Selenium speciation,
444   solubility, and mobility in land-disposed dredged sediments. Environ Sci Technol.
445   **2003**, 37,2415-2420.

446   (11)   Allaway, W. H., Cary, E. E., Ehlig, C.F. The cycling of low levels of selenium in soils,
447   plants and animals, Chapter 17 in "Selenium in Biomedicine", Muth, O. H., Oldfield, J.
448   E. and Weswig, P. H. (Eds.), AVI Publishing, Westport, CT. 1967.

449   (12)   Mitchell, K., Mason, P.D.R., Van Capellen, P., Johnson, T.M., Gill, B.C., Owens, J.D.,
450   Diaz, J., Ingall, E.D., Reichart, G.J., Lyons, T.W. Selenium as paleo-oceanographic
451   proxy: A first assessment. Geochim Cosmochim Ac. **2012**, 89, 302-317.

452   (13)   Fordyce, F.M., Guangdi, Z., Green, K., Xinping, L. Soil, grain and water chemistry in
453   relation to human selenium-responsive diseases in Enshi District, China. Appl
454   Geochem. 2000, 15(1), 117-132.

455   (14)   Qin, H., Zhu, J., Su, H. Selenium fractions in organic matter from Se-rich soils and
456   weathered stone coal in selenosis areas of China. Chemosphere. **2012**, 86(6), 626-633.

457   (15)   Wen, H., Carignan, J., Qiu, Y., Liu, S. Selenium speciation in kerogen from two
458   chinese selenium deposits: environmental implications. Environ Sci Technol. **2006,**
459   40(4), 1126-1132.

460　(16)　Matamoros-Veloza, A., Newton, R.J. and Benning, L.G. (2011). What controls
461　　　　selenium release during shale weathering? Appl Geochem. **2011**, 26, S222-S226.

462　(17)　Kulp, T.R. and Pratt, L.M. Speciation and weathering of selenium in upper cretaceous
463　　　　Chalk and shale from South Dakota and Wyoming, USA. Geochim Cosmochim Ac.
464　　　　**2004**, 68(18), 3687-3701.

465　(18)　Naveau, A., Monteil-Rivera, F., Guillon, E., Dumonceau, J. Interactions of Aqueous
466　　　　Selenium (-II) and (IV) with Metallic Sulfide Surfaces. Environ Sci Technol. **2007**,
467　　　　41(15), 5376-5382.

468　(19)　Kang, M., Chen, F., Wu, S., Yang, Y., Bruggeman, C., Charlet, L. Effect of pH on
469　　　　Aqueous Se(IV) Reduction by Pyrite. Environ Sci Technol. **2011**, 45 (7), 2704-2710.

470　(20)　Breynaert, E., Bruggeman, C., Maes, A. XANES-EXAFS Analysis of Se solid-phase
471　　　　reaction products formed upon contacting Se(IV) with FeS_2 and FeS. Environ Sci
472　　　　Technol. **2008**, 42, 3595-3601.

473　(21)　Mitchell, K. Couture, R.M., Johnson, T.M., Mason, P.R.D.. Van Cappellen, P.
474　　　　Selenium sorption and isotope fractionation: Iron(III) oxides versus iron(II) sulfides.
475　　　　Chem Geol. **2013**, 342, 21-28.

476　(22)　Strawn, D., Doner, H., Zavarin, M., McHugo, S. Microscale investigation into the
477　　　　geochemistry of arsenic, selenium, and iron in soil developed in pyritic shale materials.
478　　　　Geoderma. **2002**, 108, 237- 257.

479　(23)　Presser, T.S and Swain, W.C. Geochemical evidence for selenium mobilization by the
480　　　　weathering of pyritic shale, San Joaquin Valley, California, USA. Appl Geochem. **1990**,
481　　　　5, 703-717.

482　(24)　Brumhead D. Geology Explained in the Yorkshire Dales and on the Yorkshire Coast.
483　　　　David and Charles, London. 1979.

484　(25)　Fisher, Q.J., Wignall, P.B. Palaeoenvironmental controls on the uranium distribution in
485　　　　an Upper Carboniferous black shale (Gastrioceras listeri Marine Band) and associated
486　　　　strata. Chem Geol. **2001**, 175, 605-621.

487　(26)　Lussier C., Veiga, V., Baldwin, S. The geochemistry of selenium associated with coal
488　　　　waste in the Elk River Valley, Canada. Environ Geol. **2003**, 44, 905-913.

489　(27)　Newton, R.J., Bottrell, S.H., Dean, S.P., Hatfield, D., Raiswell, R. An evaluation of the
490　　　　use of the chromous chloride reduction method for isotopic analyses of pyrite in rocks
491　　　　and sediment. Chem Geol. **1995**, 125,317-320.

492　(28)　Calvo, C., Gillespie, R.J.,Vekris, J.E., Ng, H.N.   Title Structure of monoclinic sulphur-
493　　　　selenium Se_3S_5. Acta Crystallogra B. **1978**, B34:911-912.

494　(29)　Ryser, A.L., Strawn, D.G., Marcus, M.S., Johnson-Maynard, J.L., Gunter, M.E.,
495　　　　Moller, G. Micro-spectroscopic investigation of selenium-bearing minerals from the
496　　　　Western US Phosphate Resource Area. Geochem T. **2005**, 6(1), 1-11.

497 (30) Brostigen, G. and Kjekshus, A. Redetermined crystal structure of FeS2 (pyrite). Acta
498   Chem Scand. **1969**, 23, 2186-2188.

499 (31) Bur'yanova Z. and Komkov, A.I.   Ferroselite-a new mineral. Dokl Akad Nauk SSSR.
500   **1955**, 105,812-813 (Russian); Chemical Abstract. **1955**, 50, 9239.

501 (32) Tuttle, M.L.W.,Breit, G.N., Goldhaber, M.B. Weathering of the New Albany Shale,
502   Kentucky: II. Redistribution of minor and trace elements. App Geochem. **2009**, 24,
503   1565-1578.

504 (33) Morse, J.W. and Luther, G.W. Chemical influences on trace metal sulfide interactions
505   in anoxic sediments. Geochim Cosmochim Ac. **1999**, 63(19-20), 3373-3378.

506 (34) Diehl, S.F., Goldhaber, M.B., Koenig, A.E., Tuttle, M.L.W., and Ruppert, L.F.
507   Concentration of arsenic, selenium, and other trace elements in pyrite in appalachian
508   coals of alabama and kentucky. National Meeting of the American Society of Mining
509   and Reclamation, June 19-23, 2005. Published by ASMR, 3134 Montavesta Rd.,
510   Lexington, KY 40502. 2005.

511 (35) Berner, Z.A., Puchelt, H., Nöltner, T. and Kramar, U.T.Z. Pyrite geo-chemistry in the
512   Toarcian Posidonia Shale of south-west Germany: Evidence for contrasting trace-
513   element patterns of diagenetic and syngenetic pyrites. Sedimentology. **2013**, 60, 548–
514   573.

515 (36) Goldhaber, M.B. Sulfur-rich sediments in Treatise on Geochemistry (7) Sediments,
516   diagenesis and Sedimentary rocks. Elsevier Pergamon. 2003.

517 (37) Wilkin, R.T., Barnes, H.L., Brantley, S.L. The size distribution of framboidal pyrite in
518   modern sediments: An indicator of redox conditions. Geochim Cosmochim Ac. **1996**,
519   60(20), 3897-3912.

520 (38) Wilkin, R.T, Arthur, M.A., Dean, W.E. History of water-column anoxia in the Black
521   Sea indicated by pyrite framboid size distributions. Earth Planet Sc Lett. **1997**, 148 (5),
522   17-525.

523 (39) Wilkin, R.T. and Barnes H.L. Pyrite formation by reactions of iron monosulfides with
524   dissolved inorganic and organic sulfur species. Geochim Cosmochim Ac. **1996**, 60(21),
525   4167-4179.

526 (40) Benning, L.G., Wilkin, R.T., Barnes, H.L. Reaction pathways in the FeS system below
527   100°C. Chem Geol, **2000**, 167(1-2), 25-51.

528 (41) Love, L.G. Micro-organic material with diagenetic pyrite from the Lower Proterozoic
529   Mount Isa Shale and a Carboniferous shale. Proceeding of the Yorkshire Geological
530   Society. **1965**, 35, 187-202.

531 (42) Scheinost, A.C. and Charlet, L. Selenite reduction by mackinawite, magnetite and
532   siderite: XAS characterization of nanosized redox products. Environ Sci Technol.**2008**,
533   4,1984-1989.

534   (43) Charlet, L., Kang, M., Bardelli, F., Kirsch, R., Géhin, A., Grenèche, J.M., Chen,   F.
535   Nanocomposite Pyrite–Greigite Reactivity toward Se(IV)/Se(VI). Environ Sci Technol.
536   **2012**, 46 (9), 4869-4876.

537   (44) Howard, J. H.   Geochemistry of selenium: formation of ferroselite and selenium
538   behavior in the vicinity of oxidizing sulfide and uranium deposits. Geochim
539   Cosmochim Ac. **1977**, 41, 1665 -1678.

540   (45) Raiswell, R. and Plant, J.   The incorporation of trace elements into pyrite during
541   diagenesis of black shales, Yorkshire, England. Econ Geol. **1980**, 15, 684-699.

542   (46) Wang, Q. and Morse, J. W. Pyrite formation under conditions approximating those in
543   anoxic sediments. I. Pathway and morphology. Mar Chem. **1996**, 52, 99-121.

544   (47) Morse, J.W. and Wang, Q. Pyrite formation under conditions approximating those in
545   anoxic sediments. Mar Chem. **1997**, 57(3-4), 187-193.

546   (48) Murowchick, J.B. and Barnes, H.L.   Effects of temperature and degree of
547   supersaturation on pyrite morphology. Am Mineral. **1987**, 72, 1241-1250.

548   (49) Diener, A., Neumann, T., Kramar, U. Schild, D. Structure of selenium incorporated in
549   pyrite and mackinawite as determined by XAFS analyses. J Contam Hydrol. **2012**,
550   133, 30-39.

551   (50) Wignall, P.B. and Newton, R.   Pyrite framboid diameter as a measure of oxygen
552   deficiency in ancient mudrocks. Am J Sci. **1998**, 298, 537-552.

553   (51) Scheinost, A.C, Kirsch, R., Banerjee, D., Fernandez-Martinez, A., Zaenker, H., Funke,
554   H., Charlet, L.   X-ray absorption and photoelectron spectroscopy investigation of
555   selenite reduction by Fe-II-bearing minerals.   J Contam Hydrol. **2008**, 102(3-4), 228-
556   245.

557   (52) Bruggeman, C., Maes, A., Vancluysen, J., Vandemussele, P.   Selenite reduction in
558   Boom clay: effect of FeS2, clay minerals and dissolved organic matter. Environ Pollut.
559   **2005**,137, 209-221.

560   (53) Herbel, M.J., Blum J.S., Oremland, R.S, Borglin, S.E. Reduction of elemental selenium
561   to selenide: Experiments with anoxic sediments and bacteria that respire Se-oxyanions.
562   Geomicrobiol J. **2003**, 20, 587-602.

563   (54) Bacon, M. and Ingledew, W.J. The reductive reactions of Thiobacillus ferrooxidans on
564   sulphur and selenium. FEMS Microbiol Lett. **1989**, 58, 189-194.

565   (55) Lavergren, U. Black shale as a metal contamination source. The ESS Bulletin. **2005**,
566   3(1):18-31.

567   (56) Dudas, M.J. Enriched levels of arsenic in post-active sulphate soils in Alberta. Soil Sci
568   Soc Am J. 1984, 48(6), 1451-1452.

569   (57) Nickson, R., McArthur, J., Burgess, W., Ahmed,K. M., Ravenscroft, P., Rahman, M.
570   Mechanism of arsenic release to groundwater, Bangladesh and West Bengal. App
571   Geochem. **2000**, 15, 403-413.

572   (58)   British Geological Survey Report WC/00/19. Arsenic contamination of groundwater
573   in Bangladesh. Kinninburgh, D G and Smedley, P L Editors. 2001.

574   (59)   Sageman, B.B. and Lyons, T.W.   Geochemistry of fine-grained sediments and
575   sedimentary rocks. In: Holland, H.D. and K.K. Turekian. Treatise on geochemistry.
576   Vol. 7   Amsterdam ; London: Elsevier-Pergamon. 2003.